Applied Catalysis B: Environmental 234 (2018) 70–78

Contents lists available at ScienceDirect

Applied Catalysis B: Environmental

journal homepage: www.elsevier.com/locate/apcatb

Synthesis of a $Bi_2O_2CO_3/ZnFe_2O_4$ heterojunction with enhanced photocatalytic activity for visible light irradiation-induced NO removal

Yu Huang[a,b,*], Dandan Zhu[a], Qian Zhang[a,b], Yufei Zhang[a,b], Jun-ji Cao[a,b], Zhenxing Shen[a,c], Wingkei Ho[d], Shun Cheng Lee[e]

[a] Key Laboratory of Aerosol Chemistry and Physics, Institute of Earth Environment, Chinese Academy of Sciences, Xi'an, 710061, China
[b] State Key Lab of Loess and Quaternary Geology (SKLLQG), Institute of Earth Environment, Chinese Academy of Sciences, Xi'an, 710061, China
[c] Department of Environmental Sciences and Engineering, Xi'an Jiaotong University, Xi'an, 710049, China
[d] Department of Science and Environmental Studies, The Education University of Hong Kong, Hong Kong, China
[e] Department of Civil and Environmental Engineering, The Hong Kong Polytechnic University, Hong Kong, China

ARTICLE INFO

Keywords:
Photocatalysis
NO removal
p-n heterojunction
Internal electric field

ABSTRACT

Although bismuth subcarbonate ($Bi_2O_2CO_3$), a member of the Aurivillius-phase oxide family, is a promising photocatalyst for the removal of gaseous NO at parts-per-billion level, the large band gap of this material restricts its applications to the UV light region. The above problem can be mitigated by heterojunction fabrication, which not only broadens the light absorbance range, but also inhibits the recombination of photogenerated charge carriers. Herein, we implement this strategy to fabricate a novel $Bi_2O_2CO_3/ZnFe_2O_4$ photocatalyst for NO removal under visible light irradiation and authenticate the formation of the above *p-n* heterojunction using an array of analytical techniques. Notably, the above composite showed activity superior to those of its individual constituents, and the underlying mechanisms of this activity enhancement were probed by density functional theory calculations and photocurrent measurements. Elevated electron/hole separation efficiency caused by the presence of an internal electric field at the $Bi_2O_2CO_3/ZnFe_2O_4$ interface was identified as the main reason of the increased photocatalytic activity, with the main active species were determined as $\cdot O_2^-$ and ·OH by electron spin resonance spectroscopy. Finally, cytotoxicity testing proved the good biocompatibility of $Bi_2O_2CO_3/ZnFe_2O_4$. Thus, this work presents deep insights into the preparation and use of a green *p-n* heterojunction catalyst in various applications.

1. Introduction

In recent years, the adverse effects of nitrogen oxides (NO_x) on human health and their relevance to haze events in China have become a subject of concern [1], reflecting an increasing need for effective strategies of reducing atmospheric NO_x levels to meet the gradually rising demand for clean air. Traditional mitigation technologies such as NO_x storage and reduction, selective catalytic reduction, and physical adsorption fail to cost-effectively remove NO_x at parts-per-billion (ppb) levels [2–4], in contrast to the semiconductor photocatalysis technology, which allows the removal of low-concentration air pollutants utilizing renewable and clean solar energy. Although NO_x can be effectively removed at the ppb level via photocatalytic oxidation [5–10], the above process can not only induce direct oxidation to nitrate, but also generate the much more toxic NO_2, which highlights the importance of selecting a semiconductor material concurrently exhibiting a high NO_x conversion rate and low NO_2 selectivity. Since the photocatalytic oxidation of NO_x is a heterogeneous reaction occurring at the gaseous NO_x/catalyst phase boundary, its first step corresponds to the adsorption of NO_x on catalytic sites. Therefore, the utilization of a material exhibiting NO_x-specific adsorption at low concentration should facilitate NO_x accumulation on the catalyst surface and thus contribute to the photocatalytic oxidation reaction. Moreover, the employed photocatalysts should possess good biocompatibility, since the practical applications of nanomaterials can pose threats to human health [11]. Therefore, the exploration and design of photocatalysts with desirable physicochemical properties is extremely important to realize large-scale air purification.

Bismuth subcarbonate ($Bi_2O_2CO_3$), a member of the Aurivillius-phase oxide family, possesses a layered structure characterized by the orthogonal intergrowth of $Bi_2O_2^{2+}$ and CO_3^{2-} layers that is beneficial to the separation of photogenerated electron/hole pairs, attracting increased attention as a material for the photocatalytic degradation of organic pollutants and gaseous NO [12–14]. However, the large band

* Corresponding author at: Key Laboratory of Aerosol Chemistry and Physics, Institute of Earth Environment, Chinese Academy of Sciences, Xi'an, 710061, China.
E-mail address: huangyu@ieecas.cn (Y. Huang).

https://doi.org/10.1016/j.apcatb.2018.04.039
Received 25 February 2018; Received in revised form 4 April 2018; Accepted 17 April 2018
Available online 19 April 2018
0926-3373/

gap of $Bi_2O_2CO_3$ (~3.3 eV) renders it sensitive only to UV light, which accounts for less than 5% of solar light [15], and thus requires the response of $Bi_2O_2CO_3$ in the visible light region to be enhanced for practical environmental remediation applications. Among the various approaches adopted to solve this issue, *e.g.*, doping, morphology control, noble metal deposition, and heterojunction construction [16–19], the coupling of $Bi_2O_2CO_3$ with a narrow-band-gap semiconductor to form a heterojunction is one of the most effective ways to enhance photocatalytic performance, not only improving the efficiency of visible light utilization, but also facilitating the separation of electron-hole pairs due to energy band matching. For example, Ao et al. have prepared a CdS-loaded $Bi_2O_2CO_3$ heterojunction with extended light absorption properties and elevated charge separation efficiency, observing enhanced photocatalytic activity under visible light irradiation [20]. Besides such *n*-*n* heterojunctions, mainly designed based on energy band configuration, *p*-*n* heterojunctions have recently been extensively investigated [21–23]. The Fermi level (E_F) of a semiconductor is determined by its chemical potential at thermodynamic equilibrium [21], with *n*-type semiconductors usually having a higher E_F than *p*-type ones before contact [21]. The contact of the above semiconductors results in electron transfer from the *n*-type to the *p*-type one to reach an ultimate equilibrium state and result in E_F alignment [24]. The existence of an internal electric field (IEF) at the *p*-*n* junction formed at the contact interface of the two individual semiconductors makes this junction a special heterostructure that can significantly promote the separation of photogenerated charge carries and thus improve photocatalytic performance [21].

Spinel zinc ferrite ($ZnFe_2O_4$) is a *p*-type semiconductor with a narrow band gap (~1.9 eV) and strong visible light absorbance ability [25,26]. Unfortunately, the photocatalytic activity of pure $ZnFe_2O_4$ is relatively poor due to the rapid recombination of photogenerated electron/hole pairs [27]. However, $ZnFe_2O_4$ can be used as a sensitizer for large-bandgap semiconductors, allowing the fabrication of *p*-*n* heterojunctions with improved electron/hole pair separation efficiency [28,29]. Therefore, it is expected that a *p*-*n* heterojunction can be obtained by coupling *n*-type $Bi_2O_2CO_3$ with *p*-type $ZnFe_2O_4$. In addition, it is reasonable to assume that $ZnFe_2O_4$ is capable of strong NO surface adsorption, since Fe^{3+} ions are known to be effective adsorption sites for NO in the dark [30]. Based on the optical and adsorption properties of $ZnFe_2O_4$ as well as the E_F difference between $Bi_2O_2CO_3$ and $ZnFe_2O_4$, the $Bi_2O_2CO_3/ZnFe_2O_4$ *p*-*n* heterojunction should behave as a superior visible light–driven catalyst for NO removal.

Herein, we report that the prepared $Bi_2O_2CO_3/ZnFe_2O_4$ *p*-*n* heterojunction exhibits enhanced visible-light absorbance, NO adsorption, and charge separation properties, being an efficient visible light–driven photocatalyst for efficient NO removal at ppb levels due to IEF formation at the $Bi_2O_2CO_3/ZnFe_2O_4$ interface increasing the charge separation efficiency and inhibiting the generation of the more toxic NO_2. Moreover, cytotoxicity tests showed that the above heterojunction possessed good biocompatibility. Comprehensive characterizations were carried out to understand the physiochemical properties of the $Bi_2O_2CO_3/ZnFe_2O_4$ heterojunction, and a plausible photocatalytic mechanism was proposed.

2. Experimental

2.1. Photocatalyst preparation

All reagents were purchased from Sinopharm Chemical Reagent Co., Ltd. and used as received without further purification. Water with a resistivity exceeding 18 MΩ cm was obtained using a Millipore system.

$Bi_2O_2CO_3$ (BOC) was prepared via a hydrothermal reaction as follows [31]. Na_2CO_3 (0.46 g) was dissolved in H_2O (72 mL) upon 10-min stirring, and the obtained solution was treated with bismuth citrate (1.6 g) and agitated at ambient temperature. The resulting clear precursor solution was transferred into a 100 mL Teflon-lined autoclave, heated at 180 °C for 24 h, and naturally cooled down to room temperature. The obtained white solid was separated by centrifugation, washed with water and ethanol for five times, and dried overnight in a convection oven at 70 °C.

For the preparation of $Bi_2O_2CO_3/ZnFe_2O_4$ (BOC/ZFO) composites, BOC (0.1 g) was dispersed in H_2O (20 mL) by bath sonication to obtain a homogeneous suspension (suspension A). Subsequently, Zn $(NO_3)_2{\cdot}6H_2O$ (0.1189 g, 0.4 mmol) and $Fe(NO_3)_3{\cdot}9H_2O$ (0.3232 g, 0.8 mmol) were added to H_2O (20 mL), and the mixture was stirred to obtain a clear solution (solution B). Solution B was dropwise added to suspension A upon stirring, and the pH of the mixture was adjusted to 13 using 2 M aqueous NaOH. The above mixture was poured into a 100 mL Teflon-lined autoclave, heated at 100 °C for 6 h, and naturally cooled down to room temperature. Finally, the obtained solid was centrifuged, washed with water for five times, and dried overnight in a convection oven at 60 °C. The as-prepared composite was denoted as BOC/ZFO-(1:1) to reflect the 1:1 mass ratio of $Bi_2O_2CO_3$ and $ZnFe_2O_4$, with BOC/ZFO-(1:0.1) and BOC/ZFO-(1:5) composites prepared in an identical way. For comparison, pure $ZnFe_2O_4$ was also prepared using the above method without the addition of BOC.

2.2. Photocatalyst characterization

Powder X-ray diffraction (XRD) patterns (X'pert Pro, PANalytical Corp., the Netherlands) were recorded at a scan rate of 0.017° min^{-1} using Cu K_α radiation. Transmission electron microscopy (TEM) and high-resolution TEM (HRTEM) analyses were carried out using a JEOL 2010 microscope (JEOL Corp., Japan). X-ray photoelectron spectroscopy (XPS) measurements were performed on an Escalab 250 Xi spectrometer (Thermo Scientific, USA), and binding energies were calibrated using the C 1*s* peak at 284.6 eV as a reference. Nitrogen sorption experiments were conducted at 77 K using an automated physisorption analyzer (Gemini VII 2390, Micromeritics Instrument Corp., USA), and specific surface areas and pore size distributions were determined employing the Brunauer–Emmett–Teller (BET) equation and the Barrett–Joyner–Halenda method, respectively. UV–vis diffuse reflectance spectroscopy (DRS) surveys were performed on an Agilent Cary 100 UV–vis spectrometer (Agilent Corp., USA) with $BaSO_4$ as a reference. NO temperature-programmed desorption (TPD) experiments were conducted on a chemisorption analyzer (PCA 1200, BJbuilder, China) using 50 mg samples. Prior to TPD analyses, samples were pretreated in a stream of N2 at 100 °C for 30 min. After cooling to room temperature, the thus treated samples were exposed to a stream of NO (40 mL min–1) at room temperature for 30 min, and the temperature was increased to 600 °C at a rate of 10 °C min–1 in a flow of He (30 mL min–1) for NO desorption. Thermogravimetric analysis (TGA; STA 449 F5, Netzsch, Germany) was conducted at a heating rate of 10 °C min–1 in ambient atmosphere. Electron spin resonance (ESR; ER200-SRC, Bruker, Germany) spectra were recorded at ambient temperature under 12 min visible light irradiation, with the corresponding samples prepared by adding photocatalysts into a 5,5-dimethyl-1-pyrroline-*N*-oxide (DMPO)-containing solution (CH_3OH dispersion for $\cdot O_2^-$ and aqueous dispersion for $\cdot OH$ observation).

2.3. NO removal testing

The activity of as-prepared photocatalysts for NO removal was evaluated in a continuous flow reactor at room temperature. The rectangular stainless steel chamber of the reactor had a top quartz glass panel and featured a total volume of 4.5 L (30 cm × 15 cm × 10 cm). A 9-cm-diameter glass dish was coated with 0.1 g samples by evaporating the corresponding photocatalyst-containing suspensions at 70 °C and placed at the center of the chamber. The initial NO gas (400 ppb) was obtained by diluting 100 ppm NO sourced from a compressed gas cylinder (N_2 balance) with air supplied by a zero-air generator (Model 1001, Sabio Instruments LLC, USA), and the flow rate of the air/NO

mixture was controlled at 3 L min^{-1}. A commercial 300 W xenon lamp with a 420 nm cutoff filter (Microsolar 300, Perfectlight, China) was vertically placed above the reactor as a light source. The sample dish was continuously exposed to the above gas stream, and the xenon lamp was turned on after a constant NO concentration was achieved in the dark after ~30 min, with the concentrations of NO, NO_2, and NO_x measured by an NO_x analyzer (Model 42c, Thermo Environmental Instruments Inc., USA) throughout the photocatalytic test. The NO removal efficiency was determined as $(1 - C/C_0) \times 100\%$, where C and C_0 represent the NO outlet concentration at a given time and the initial inlet concentration (ppb), respectively.

2.4. Photoelectrochemical measurements

Transient photocurrents were evaluated using an electrochemical workstation (Parstat 4000, Princeton, USA) in a conventional three-electrode cell, with a Pt plate and a Ag/AgCl electrode used as counter and reference electrodes, respectively. To fabricate the working electrode, solid samples (10 mg) were dispersed in ethanolic Nafion (1 mL, 1 wt%) by bath sonication to obtain homogeneous suspensions that were dropt-cast onto fluorine-doped tin oxide conducting glass and dried at room temperature to produce films. Photocurrent density–time curves were measured at 0.2 V *vs.* Ag/AgCl in 0.5 M Na_2SO_3 solution at room temperature under LED lamp irradiation (λ = 420 nm).

2.5. Density functional theory (DFT) calculations

All first-principle DFT calculations were implemented using the Cambridge Sequential Total Energy Package (CASTEP) code and the plane-wave Vanderbilt-type ultrasoft pseudopotential approach [32]. The supercell models of the bulk BOC and ZFO were built, and the supercells of 1 × 1 × 1 and 2 × 1 × 1 were used for BOC and ZFO, respectively. The crystal models of the BOC/ZFO heterojunction with the interfaces composed of BOC (110) and ZFO (220) lattice planes were also constructed. The generalized gradient approximation with the Perdew–Burke–Ernzerhof functional was used to account for exchange correlation potentials and electron-electron interactions [33]. The Brillouin zones were separately sampled at 1 × 3 × 1 Monkhorst-Pack *k*-points for the BOC/ZFO heterojunction models. The kinetic cutoff energy was set to 380 eV for all calculations, and the self-consistent field convergence criterion was set to 2.0×10^{-6} eV. For geometry optimization, the energy change, residual force, stress and displacement convergence criteria were chosen to be less than 2.0×10^{-5} eV atom^{-1}, 0.05 eV Å^{-1}, 0.1 GPa and 0.002 Å, respectively. Charge transfer between BOC and ZFO was evaluated based on electron density difference (EDD) maps and Mulliken population analysis (MPA) performed using a 2 × 4 × 2 mesh.

2.6. Cytotoxicity tests

The cytotoxicity of BOC/ZFO-(1:1) to A549 cells was evaluated by a standard methylthiazolydiphenyltetrazolium bromide (MTT) assay. A549 cells initially cultured for 12 h in an incubator (37 °C, 5% CO_2) were seeded in 96 well U-bottom plates at a density of 5×10^4 – 1×10^5 cell mL^{-1} (200 μL per well) and incubated with different concentrations of BOC/ZFO-(1:1) (0.5, 5, 10, 25, 50, 100, 200, and 400 μg mL^{-1}). After 24 h culturing with BOC/ZFO-(1:1), 15 μL of the MTT solution (normal saline or 1 mg mL^{-1} phosphate buffer solution) was added to each sample, which were further incubated at 37 °C for 4 h. The culture medium was discarded, and dimethyl sulfoxide (150 μL) was added upon 10 min shaking to dissolve formazan. Optical densities (ODs) were measured at 490 nm using a microplate reader, and cell viability was estimated as

$$\text{Cell viability (\%)} = OD_{treated} / OD_{control} \times 100\% \quad (1)$$

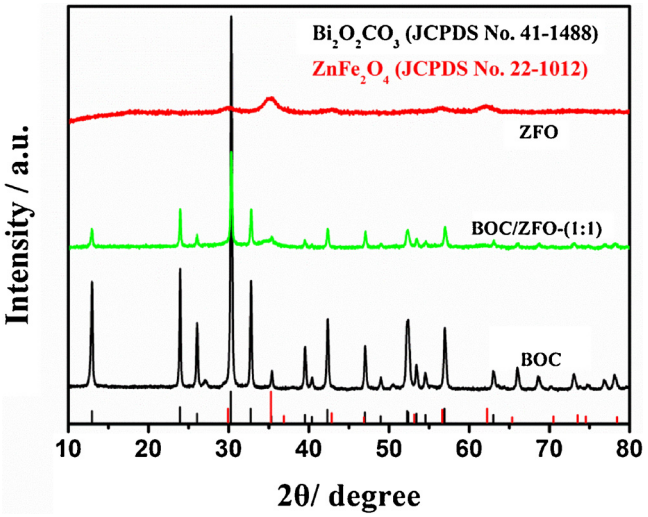

Fig. 1. XRD patterns of BOC, BOC/ZFO-(1:1), and ZFO.

where $OD_{control}$ is the optical density obtained in the absence of BOC/ZFO-(1:1), and $OD_{treated}$ is the value obtained in the presence of BOC/ZFO-(1:1). Additionally, the same cytotoxicity test was also conducted for P25 as a control.

3. Results and discussion

3.1. Physicochemical characterization

3.1.1. Crystal structures and chemical compositions

The crystal structures of as-prepared BOC, ZFO, and BOC/ZFO-(1:1) were determined by XRD (Fig. 1). All diffraction peaks of pure BOC could be well indexed to tetragonal $Bi_2O_2CO_3$ (JCPDS No. 41-1488), with their sharp and intense nature being indicative of very high crystallinity [17]. For pure ZFO, the diffraction peaks at 2θ = 29.9°, 35.2°, 56.6°, and 62.2° were assigned to the (220), (311), (511), and (440) reflections of $ZnFe_2O_4$ (JCPDS No. 22-1012), respectively [34], with the average crystallite size estimated as 13.1 nm according to the Scherrer equation. The similarity between the diffraction peaks of BOC/ZFO-(1:1) and those of BOC indicated that the latter compound was partially covered by ZFO in the former composite, with the absence of ZFO peaks ascribed to its low crystallinity. For comparison, the XRD patterns of BOC/ZFO-(1:0.1) and BOC/ZFO-(1:5) are shown in Fig. S1. The peaks of BOC/ZFO-(1:0.1) resembled those of BOC, while BOC/ZFO-(1:5) showed only weak BOC peaks due to the excessive coverage of BOC by ZFO, with $ZnFe_2O_4$ peaks being clearly identifiable at increased ZFO loading. No other impurity peaks were observed, suggesting that all as-prepared samples were highly pure. Thus, the aforementioned results confirmed the successful fabrication of BOC/ZFO composites.

The surface chemical states and elemental compositions of BOC, ZFO, and BOC/ZFO-(1:1) were probed by XPS. Survey spectra in Fig. 2a show the presence of three elements in BOC and reveal the simultaneous existence of Bi, C, O, Zn, and Fe in BOC/ZFO-(1:1), indicating the partial coverage of BOC by ZFO and being in agreement with the results of XRD analysis. Fig. 2b shows the C 1 s spectra of BOC and BOC/ZFO-(1:1), with the peaks at 284.6 and 285.5 eV (observed for both materials) assigned to adventitious carbon species, whereas that at 288.6 eV was attributed to CO_3^{2-} in BOC and shifted to higher binding energies in BOC/ZFO-(1:1) [35–37]. Fig. 2c features two strong characteristic peaks at 158.9 and 164.2 eV that were ascribed to Bi $4f_{5/2}$ and Bi $4f_{7/2}$ transitions of Bi^{3+} in BOC, respectively; whereas both of these peaks shifted to higher binding energies (by ~0.1 eV) for BOC/ZFO-(1:1) [23]. In O 1*s* spectrum of BOC (Fig. 2d), three peaks centered at 530.2,

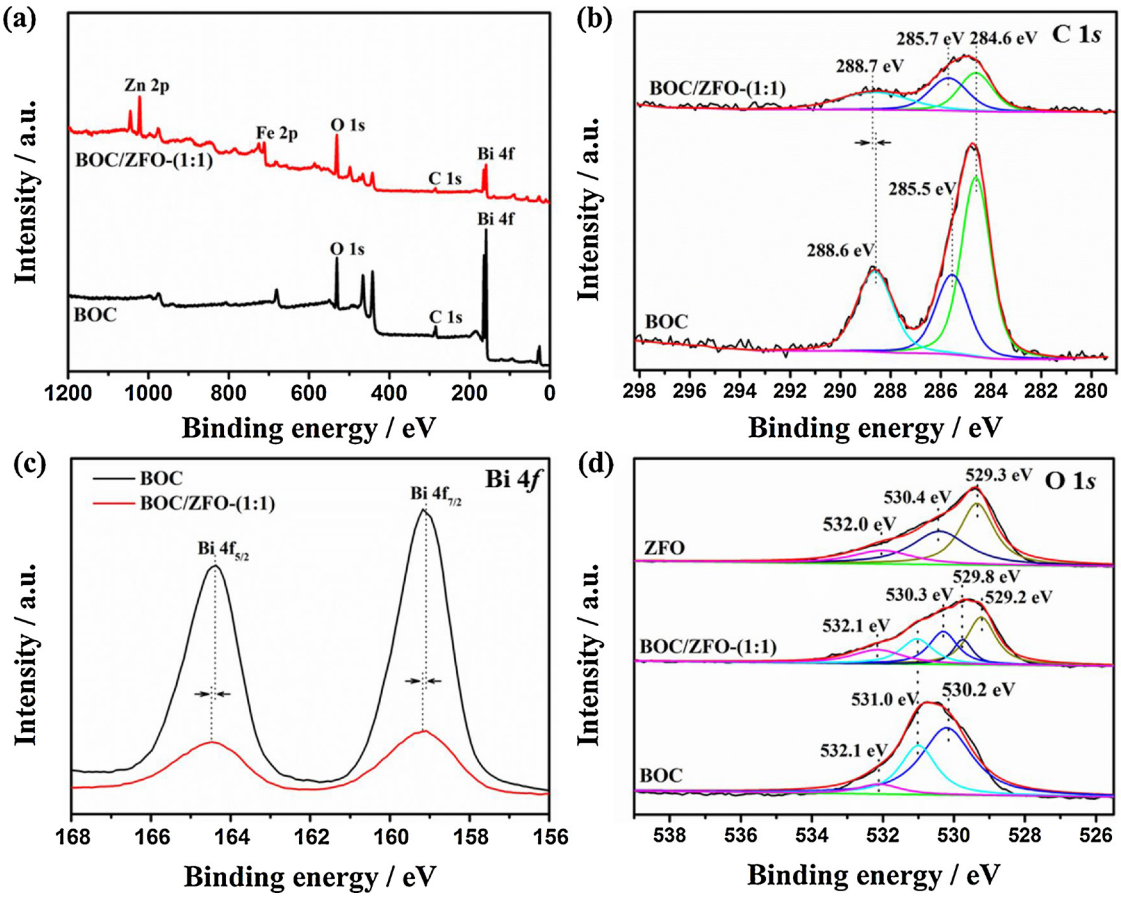

Fig. 2. XPS survey spectra of BOC and BOC/ZFO-(1:1) (a); high-resolution C 1 s (b), Bi 4f (c), and O 1 s (d) spectra of the corresponding samples.

531.0, and 532.1 eV were assigned to Bi—O bonds in BOC, carbonate species, and absorbed H_2O (or surface —OH), respectively [13,38,39]. In the case of ZFO, the peaks observed at 529.3 and 530.4 eV were assigned to Fe—O and Zn—O bonds in ZFO, respectively [40]. As for BOC/ZFO-(1:1), the O 1*s* spectrum contains five shoulders, among which the peak drift towards higher binding energies at 530.3 eV of Bi—O bonds as well as those shift towards lower binding energies at 529.2 and 529.8 eV of Fe—O and Zn—O bonds could be clearly observed. Generally, XPS binding energy is negatively correlated with surface electron density [41,42]. The decreased electron density could lower the electron screening effect, thereby resulting in the elevated binding energy. Thus, the enhancement of binding energies of C, Bi, and O peaks observed for BOC in BOC/ZFO-(1:1) was ascribed to the reduced electron concentration on its surface, which might be induced by electron transfer from BOC to ZFO. The electron transfer direction between BOC and ZFO was further evidenced by DFT calculations thereinafter. Therefore, the above results confirmed the existence of a strong interaction between BOC and ZFO and suggested the formation of a BOC/ZFO heterojunction.

3.1.2. Morphological characterization

Morphological structures and crystallographic features of as-prepared BOC, ZFO, and BOC/ZFO-(1:1) were characterized by TEM and HRTEM. As shown in Fig. 3a, BOC featured plate-like nanostructures with sizes of 150–200 nm. The corresponding HRTEM image (Fig. 3b) displays clear lattice fringes with interplanar spacings of 0.273 and 0.272 nm, which were ascribed to the (110) and (–110) crystal planes of orthorhombic $Bi_2O_2CO_3$ (JCPDS No. 41-1488), respectively, suggesting its high crystallinity [23]. Fig. 3c depicts a representative TEM image of ZFO, revealing that it comprised spherical particles (9 ± 2 nm in size), in accordance with the results of XRD analysis. The corresponding HRTEM image in Fig. 3d shows clear lattice fringes and interplanar distances of 0.298 and 0.254 nm, which correspond to the (220) and (311) crystal planes of cubic spinel $ZnFe_2O_4$ (JCPDS No. 22-1012), respectively [43]. Fig. 3e shows the TEM image of BOC/ZFO-(1:1), revealing the partial deposition of ZFO onto the surface of BOC. Fig. 3f displays crystal lattice fringes in distinct regions of the above composite, with the interplanar spacings of 0.273 and 0.272 nm assigned to the (110) and (–110) crystal planes of $Bi_2O_2CO_3$, whereas the *d*-spacings of 0.298 and 0.254 nm were indexed to the (220) and (311) crystal planes of $ZnFe_2O_4$, respectively. Moreover, the above image demonstrated that the BOC and ZFO phases were in close contact with each other to form an intimate interface.

3.2. Photocatalytic activity

The photocatalytic NO removal activities of BOC, ZFO, and BOC/ZFO composites were investigated under visible light irritation ($\lambda \geq 420$ nm) at ambient temperature. Fig. 4a displays the NO removal extent over different photocatalysts as a function of irradiation time, revealing that pure BOC showed poor photocatalytic activity. Moreover, despite showing a certain activity, pure ZFO exhibited a suboptimal photocatalytic performance owing to the rapid recombination of photogenerated electrons and holes [27]. Conversely, BOC/ZFO-(1:0.1) exhibited enhanced photocatalytic NO removal activity compared to that of its individual constituents, with the best performance observed for BOC/ZFO-(1:1). BOC/ZFO-(1:5) exhibited lower activity than the 1:1 composite, which was explained by the excess ZFO in the former hindering charge transfer between BOC and ZFO. The yield of the more toxic NO_2 intermediate was monitored throughout the photocatalytic process (Fig. 4b), being quite low over BOC and ZFO (< 20 ppb). Coupling of ZFO with BOC significantly inhibited NO_2

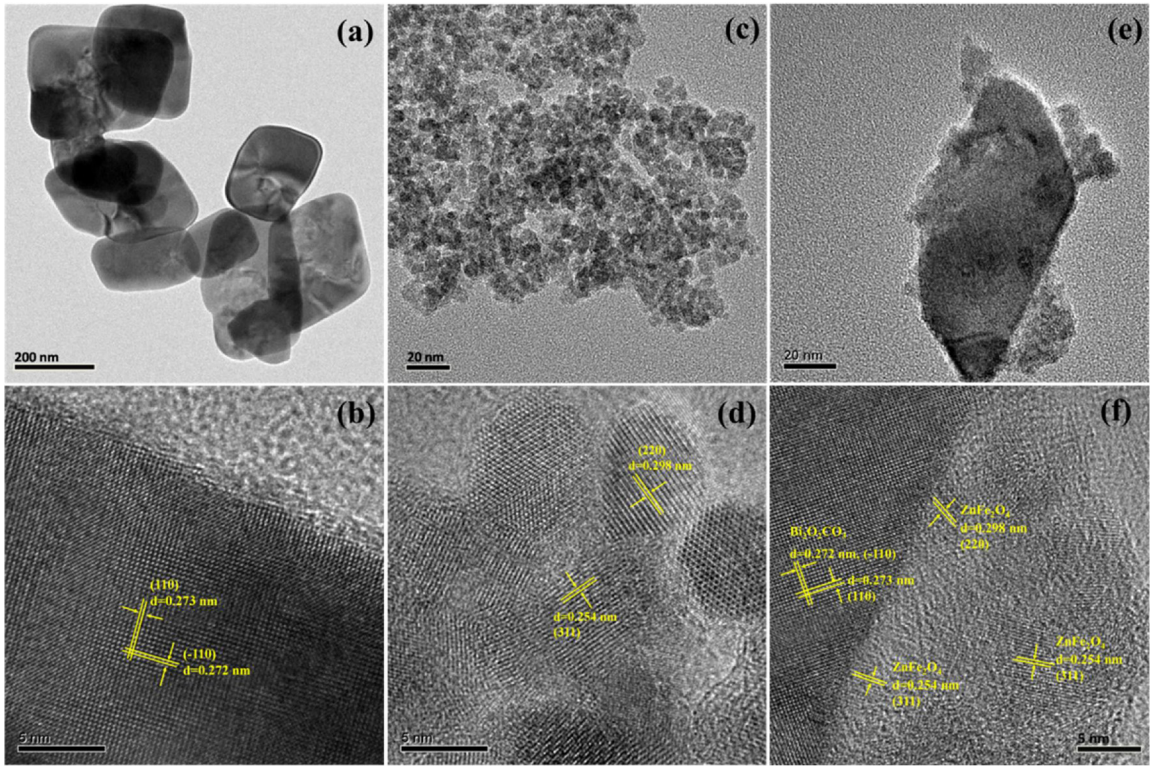

Fig. 3. TEM (a, c, e) and HRTEM (b, d, f) images of BOC (a, b), ZFO (c, d), and BOC/ZFO-(1:1) (e, f).

generation, *i.e.*, no NO_2 was produced when BOC/ZFO-(1:1) was utilized, which indicated the high potential of heterostructured BOC/ZFO composites for air purification. As demonstrated in Fig. 4a, the photocatalytic activity of all heterostructured photocatalysts did not show any decay during NO removal. Repeated photocatalytic NO removal experiments conducted over BOC/ZFO-(1:1) (Fig. S2) showed that the activity of this composite slightly decreased after four-fold recycling, implying that the above heterojunction possessed superior stability.

3.3. Photocatalytic mechanism analyses

3.3.1. Textural, optical, and electric properties

In view of the fact that the textural and optical properties of photocatalysts impact their activity, nitrogen adsorption isotherm and DRS measurements were performed to evaluate the effects of specific surface area and light absorbance capacity on photocatalytic performance, respectively.

Fig. S3 displays the nitrogen adsorption isotherms and pore size distributions of BOC, ZFO, and BOC/ZFO-(1:1). Both ZFO and BOC/ZFO-(1:1) displayed type-VI isotherms with evident hysteresis loops characteristic of mesoporous materials, while BOC showed a type-III isotherm typical of macroporous surfaces [44]. As illustrated in Fig. S3b, ZFO and BOC/ZFO-(1:1) exhibited mesopores with diameters of 2.7 and 2.8 nm, respectively, while BOC featured a bimodal size distribution of macropores (inset of Fig. S3b), in accordance with the insights gained from the analysis of nitrogen sorption isotherms. BET specific surface areas (S_{BET}) and pore volumes for BOC, ZFO, and BOC/ZFO-(1:1) are listed in Table S1, with the larger S_{BET} of BOC/ZFO-(1:1) compared to that of BOC suggesting that the former material possessed a larger amount of active sites and thus exhibited a higher photocatalytic activity. However, although BOC/ZFO-(1:1) exhibited a lower S_{BET} than that of pure ZFO, its photocatalytic performance was higher, which implied that S_{BET} does not account for the elevated photocatalytic activity of BOC/ZFO-(1:1).

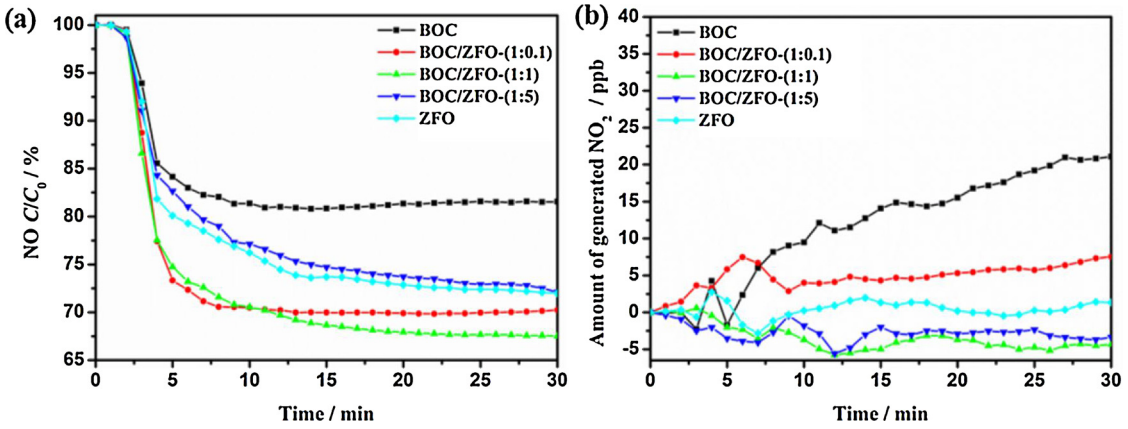

Fig. 4. Efficiency of photocatalytic NO removal (a) and amount of generated NO_2 (b) as functions of visible light ($\lambda \geq 420$ nm) irradiation time for BOC, ZFO, and BOC/ZFO composites.

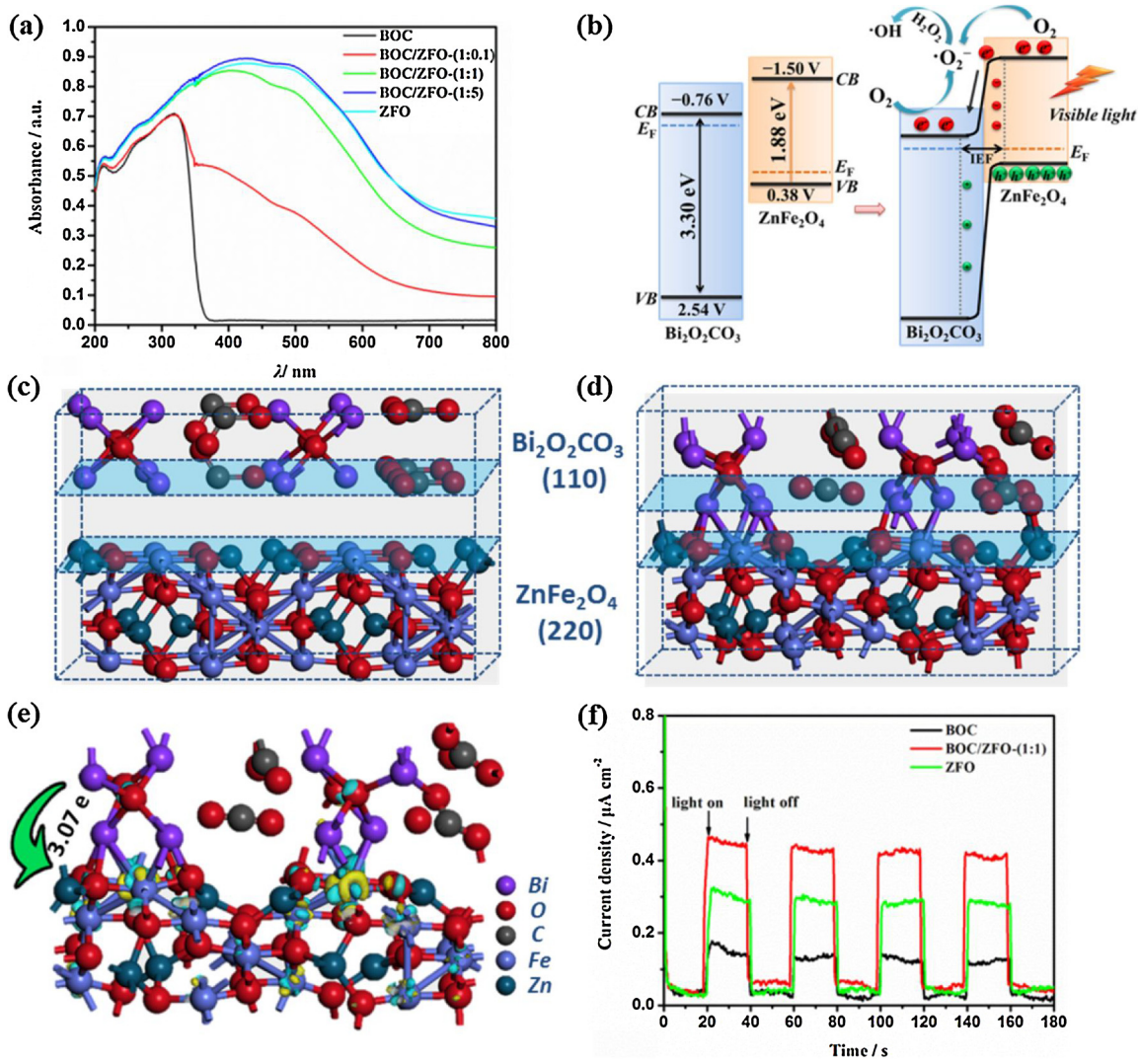

Fig. 5. (a) UV–vis DRS spectra of BOC, ZFO, and BOC/ZFO composites. (b) Energy band structure of BOC and ZFO before and after contact and the possible charge transfer process for visible light–irradiated BOC/ZFO-(1:1). Constructed (c) and optimized (d) crystal structures of the BOC/ZFO interface. (e) Calculated EDD plot for the BOC/ZFO interface at an isovalue of 0.1 e Å^{-3}, with blue and yellow regions representing electron density accumulation and depletion, respectively. (f) Current–time curves of BOC, ZFO, and BOC/ZFO-(1:1) recorded in 0.5 M Na_2SO_3 under visible light irradiation (λ = 420 nm) (For interpretation of the references to colour in this figure legend, the reader is referred to the web version of this article).

Fig. 5a shows the UV–vis DRS spectra of BOC, ZFO, and BOC/ZFO composites, revealing that pure BOC absorbs only in the UV region, whereas pure ZFO exhibits a broad absorption peak in the visible light region. Notably, the deposition of ZFO onto BOC to afford BOC/ZFO resulted in significantly enhanced absorbance intensity in the visible light region, with this increase being positively correlated with ZFO content and thought to promote photocatalytic activity. However, contrary to our expectations, the highest activity was observed for BOC/ZFO-(1:1) and not for BOC/ZFO-(1:5), which implies that surface area and light absorbance capacity are not the only factors determining photocatalytic activity.

The band gap energies (E_gs) of BOC and ZFO were calculated according to the following equation [45]:

$$\alpha h\nu = A(h\nu - E_g)^{n/2} \quad (2)$$

where α, h, ν, and A denote the absorption coefficient, Plank constant, light frequency, and a constant, respectively, and n is determined by the type of semiconductor optical transition, equaling four for direct transitions and unity for indirect ones [45]. For BOC, the $(\alpha h\nu)^{1/2}$ vs. $h\nu$ plot constructed assuming $n = 4$ (Fig. S4a) allowed the E_g of BOC to be determined as 3.30 eV, with the corresponding value of ZFO for $n = 1$ determined as 1.88 eV by a similar method (Fig. S4b). Conduction band edges (E_{CB}s) and valence band edges (E_{VB}s) of BOC and ZFO were determined to further shed light on the photocatalytic mechanism. According to previous reports, the E_{CB} of $Bi_2O_2CO_3$ equals –0.76 V (vs. NHE) [46], which allows the E_{VB} of $Bi_2O_2CO_3$ to be calculated as 2.54 V (vs. NHE) from $E_{CB} = E_{VB} - E_g$. Similarly, the E_{CB} and E_{VB} of $ZnFe_2O_4$ were determined as –1.50 and 0.38 V (vs. NHE), respectively [47]. According to the E_{CB} and E_{VB} values obtained for $Bi_2O_2CO_3$ and $ZnFe_2O_4$, the energy band structure of these compounds before contact is illustrated in Fig. 5b (left). Given that $Bi_2O_2CO_3$ is an n-type semiconductor, and $ZnFe_2O_4$ is a p-type semiconductor, these species should exhibit different E_F positions [21,48]. However, upon contact of these materials, electrons are transferred from $Bi_2O_2CO_3$ (with a higher E_F) to $ZnFe_2O_4$ (with a lower one), as evidenced by the results of XPS analysis, until both E_Fs ultimately reach an equilibrium state. This phenomenon can cause band bending for both semiconductors, and $ZnFe_2O_4$/$Bi_2O_2CO_3$ p-n junctions are thus expected to form an IEF at the contact interface, as shown in Fig. 5b (right).

To further demonstrate the origin of charge transfer at the BOC/ZFO heterojunction interface, the EDD of this heterojunction was evaluated

by density functional theory calculations. The crystal models of BOC/ZFO composites featured interfaces composed of BOC (110) and ZFO (220) lattice planes is illustrated in Fig. 5c, with Fig. 5d showing the optimized BOC/ZFO interface after model relaxation. The calculated EDD plot is shown in Fig. 5e. As noted above, the obtained EDD confirms that charge transfer occurs at the BOC/ZFO interface. Furthermore, MPA charge distribution data indicates that about 3.07 electrons transfer from BOC to ZFO, in accordance with the results of XPS analysis. Therefore, the $ZnFe_2O_4/Bi_2O_2CO_3$ *p-n* junctions facilitate the formation of an IEF at the contact interface and thus promote interfacial charge separation.

The mechanisms of charge transfer/separation under visible light irradiation proposed on the basis of the abovementioned analyses are illustrated in Fig. 5b (right). When BOC/ZFO-(1:1) was exposed to visible light irradiation ($\lambda \geq 420$ nm), electron/hole pairs were generated over ZFO. Owing to the existence of an IEF at the BOC/ZFO interface, the photogenerated electrons in the ZFO conduction band could be transferred to that of BOC due to the more positive E_{CB} of the latter, whereas the photogenerated holes remained in the ZFO valence band. Consequently, the coupling of ZFO and BOC facilitated charge transfer and thus enhanced the separation efficiency of photogenerated electrons and holes, as verified by photocurrent measurements (Fig. 5f). The highest photocurrent density was obtained for BOC/ZFO-(1:1), suggesting that the above composite possessed the highest electron/hole separation efficiency.

Based on the above results, we can conclude that the elevated electron/hole separation efficiency caused by the presence of an internal electric field at the BOC/ZFO interface was identified as the main reason of the increased photocatalytic activity observed for BOC/ZFO-(1:1). Previous reports have also demonstrated that the separation efficiency of photogenerated charge carriers played a significant role in the photocatalytic activity [49–51].

3.3.2. NO adsorptive properties

Since the adsorption of NO is critical for its further photocatalytic oxidation, the NO adsorption-desorption properties of BOC/ZFO-(1:1) and pure BOC were analyzed by TPD experiments (Fig. S5). As demonstrated in Fig. S5a, the intensity of desorption peaks for BOC/ZFO-(1:1) at $T < 320$ °C exceeded that of pure BOC, suggesting that the former material exhibited a higher NO adsorption capability in the dark, with the adsorbed NO being easily desorbed within the investigated temperature range. The strong peak at ~390 °C (onset temperature ≈300 °C) was ascribed to the decomposition of BOC, as confirmed by the similar TPD profile observed for BOC in the absence of NO pre-adsorption (inset of Fig. S5a). Thermogravimetric analysis of BOC (Fig. S5b) indicated that decomposition started at ~300 °C. Thus, the above results indicated that the coupling of ZFO with BOC to produce BOC/ZFO-(1:1) resulted in enhanced NO adsorption capability, benefitting photocatalytic NO oxidation.

3.3.3. Reactive radical production

The mechanism of photocatalytic NO removal over BOC/ZFO-(1:1) was further investigated employing ESR spectroscopy to detect reactive oxygen species ($\cdot O_2^-$ and ·OH) generated over different catalysts under visible light irradiation. As shown in Fig. 6a, strong characteristic signals of $\cdot O_2^-$ were detected in a methanolic dispersion of BOC/ZFO-(1:1), whereas peaks of ·OH were observed in the corresponding aqueous dispersion, as displayed in Fig. 6b. The high intensity of both $\cdot O_2^-$ and ·OH peaks indicated that these species might play important roles in the photocatalytic removal of NO. In addition, BOC/ZFO-(1:1) displayed much stronger $\cdot O_2^-$ and ·OH signals than pure BOC and ZFO, which indicated that the coupling of BOC with ZFO promoted the generation of the above radicals. The photogenerated electrons in the conduction bands of BOC and ZFO could be captured by O_2 to produce large amounts of $\cdot O_2^-$ due to $Bi_2O_2CO_3$ and $ZnFe_2O_4$ having E_{CB}s more negative than the redox potential of the $O_2/\cdot O_2^-$ system (−0.33 V) [52]. As for ·OH, the valence band energy of ZFO was more negative than the redox potential of the $OH^-/\cdot OH$ system (2.38 V) [52], with the photogenerated holes in the valence band thus not being able to oxidize OH^- to ·OH. Therefore, the ·OH radicals detected by ESR were believed to be formed via the route of $\cdot O_2^- \rightarrow H_2O_2 \rightarrow \cdot OH$ [53].

Based on the obtained results, the following mechanism of photocatalytic NO removal was proposed:

$$ZnFe_2O_4 + h\upsilon \rightarrow ZnFe_2O_4\ (h^+ + e^-)\ (\lambda \geq 420\ nm) \quad (3)$$

$$e^-\ (ZnFe_2O_4) \rightarrow e^-\ (Bi_2O_2CO_3) \quad (4)$$

$$e^-\ (ZnFe_2O_4/Bi_2O_2CO_3) + O_2 \rightarrow \cdot O_2^- \quad (5)$$

$$\cdot O_2^- + NO \rightarrow NO_3^- \quad (6)$$

$$\cdot O_2^- + 2H^+ + e^- \rightarrow H_2O_2 \quad (7)$$

$$H_2O_2 + e^- \rightarrow \cdot OH + OH^- \quad (8)$$

$$NO + 2\cdot OH \rightarrow NO_2 + H_2O \quad (9)$$

$$NO_2 + \cdot OH \rightarrow NO_3^- + H^+ \quad (10)$$

The irradiation of BOC/ZFO-(1:1) by visible light ($\lambda \geq 420$ nm) resulted in the photogeneration of electron/hole pairs over $ZnFe_2O_4$ (Eq. (3)). Due to the presence of an IEF, the electrons in the conduction band of $ZnFe_2O_4$ could migrate to that of $Bi_2O_2CO_3$ (Eq. (4)). Subsequently, electrons in both conduction bands reacted with molecular O_2 to afford $\cdot O_2^-$ (Eq. (5)), which could directly oxidize NO to NO_3^- (Eq. (6)) or be converted into ·OH via the $\cdot O_2^- \rightarrow H_2O_2 \rightarrow \cdot OH$ route (Eqs. (7) and (8)), with the produced ·OH being able to further oxidize NO to NO_3^- (Eqs. (9) and (10)).

3.4. Biocompatibility

In order to be suitable for large-scale applications, semiconductor photocatalysts should exhibit good biocompatibility. In view of the above, BOC/ZFO-(1:1) was subjected to cytotoxicity testing. Fig. 7 shows that a dose-dependent decrease of cell number was observed for P25 dosages of 0.5–400 μg mL^{-1}. Specifically, no significant change was observed at concentrations of 0.5–5 μg mL^{-1}, whereas cell growth inhibition was observed at levels of 10–400 μg mL^{-1}. A roughly 50% reduction of cell viability was observed at the highest P25 concentration of 400 μg mL^{-1}, whereas BOC/ZFO-(1:1) did not cause any significant reduction of cell viability at concentrations of 0.5–400 μg mL^{-1}. Thus, as-prepared BOC/ZFO-(1:1) was more biocompatible than P25, exhibiting a great potential for practical applications.

4. Conclusions

Herein, we successfully prepared a novel $Bi_2O_2CO_3/ZnFe_2O_4$ *p-n* heterojunction photocatalyst and utilized it for the photocatalytic removal of NO under visible light irradiation, showing that the heterostructured BOC/ZFO-(1:1) composite not only exhibited superior photocatalytic NO removal activity (exceeding that of pure BOC and ZFO), but also featured good stability and low NO_2 selectivity. The high photocatalytic activity was mainly attributed to the enhanced separation efficiency of photogenerated electron/hole pairs due to the existence of an IEF at the BOC/ZFO contact interface, whereas ESR spectroscopy showed that both $\cdot O_2^-$ and ·OH were the major active species generated during the photocatalytic process. In addition, BOC/ZFO-(1:1) displayed high biocompatibility, which increased its practical application scope.

Notes

The authors declare no competing financial interest.

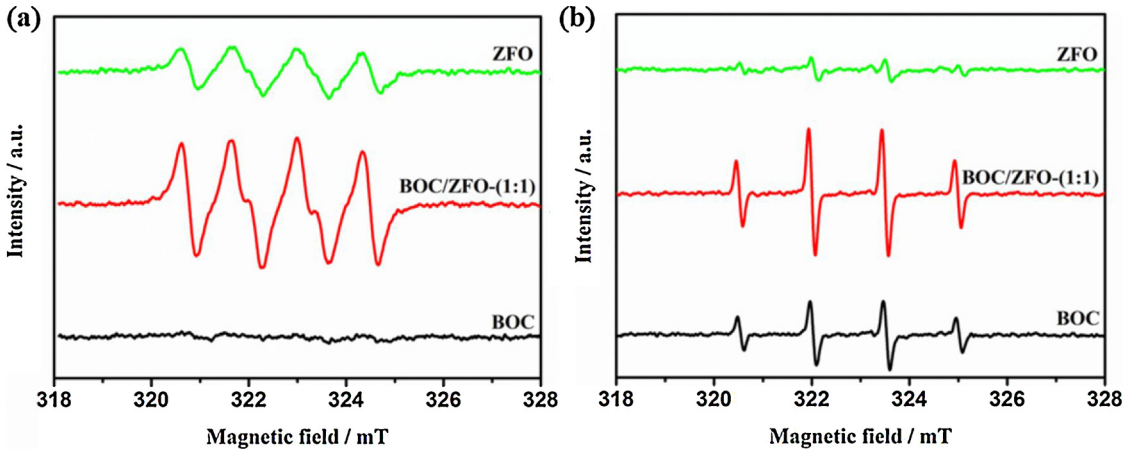

Fig. 6. ESR spectra of DMPO-trapped $\cdot O_2^-$ in methanolic dispersions (a) and of DMPO-trapped ·OH in aqueous dispersions (b) of BOC, ZFO, and BOC/ZFO-(1:1) subjected to 12 min visible light irradiation.

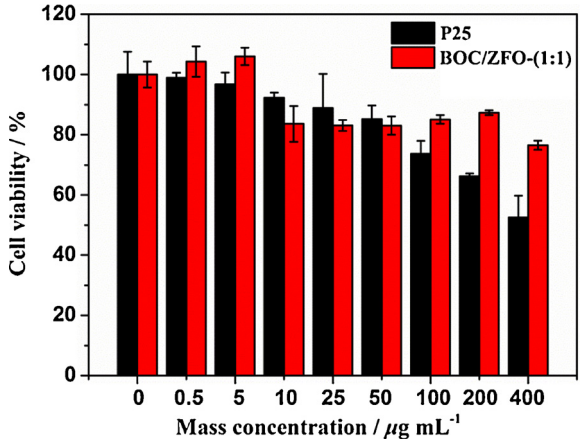

Fig. 7. Viability of A549 cells after 24 h exposure to P25 and BOC/ZFO-(1:1).

Acknowledgements

This research was financially supported by the National Key Research and Development Program of China (2016YFA0203000), the State Key Lab of Loess and Quaternary Geology (SKLLQGPY1605) and the National Science Foundation of China (Nos. 41401567 and 41573138). It was also partially supported by the Key Project of International Cooperation of the Chinese Academy of Sciences (GJHZ1543) and the Research Grants Council of Hong Kong (PolyU 152083/14E). Yu Huang is also supported by the "Hundred Talent Program" of the Chinese Academy of Sciences.

Appendix A. Supplementary data

Supplementary material related to this article can be found, in the online version, at doi:https://doi.org/10.1016/j.apcatb.2018.04.039.

References

[1] R.J. Huang, Y. Zhang, C. Bozzetti, K.F. Ho, J.J. Cao, Y. Han, K.R. Daellenbach, J.G. Slowik, S.M. Platt, F. Canonaco, P. Zotter, R. Wolf, S.M. Pieber, E.A. Bruns, M. Crippa, G. Ciarelli, A. Piazzalunga, M. Schwikowski, G. Abbaszade, J. Schnelle-Kreis, R. Zimmermann, Z. An, S. Szidat, U. Baltensperger, I. El Haddad, A.S. Prevot, Nature 514 (2014) 218–222.
[2] Y. Peng, W. Si, J. Luo, W. Su, H. Chang, J. Li, J. Hao, J. Crittenden, Environ. Sci. Technol. 50 (2016) 6442–6448.
[3] Y. Cheng, J. Liu, Z. Zhao, Y. Wei, W. Song, C. Xu, Environ. Sci.: Nano 4 (2017) 1168–1177.
[4] H.Y. Huang, R.T. Yang, Langmuir 17 (2001) 4997–5003.
[5] Z. Zhao, W. Zhang, Y. Sun, J. Yu, Y. Zhang, H. Wang, F. Dong, Z. Wu, J. Phys. Chem. C 120 (2016) 11889–11898.
[6] W. Wang, Y. Huang, X. Zhang, J.-j. Cao, W. Ho, S.C. Lee, Aerosol Sci. Eng. 1 (2017) 33–40.
[7] Q. Zhang, Y. Huang, L. Xu, J.J. Cao, W. Ho, S.C. Lee, ACS Appl. Mater. Inter. 8 (2016) 4165–4174.
[8] Z. Wang, Y. Huang, W. Ho, J. Cao, Z. Shen, S.C. Lee, Appl. Catal. B: Environ. 199 (2016) 123–133.
[9] Y. Gao, Y. Huang, Y. Li, Q. Zhang, J.-j. Cao, W. Ho, S.C. Lee, ACS Sustain. Chem. Eng. 4 (2016) 6912–6920.
[10] X. Ding, W. Ho, J. Shang, L. Zhang, Appl. Catal. B: Environ. 182 (2016) 316–325.
[11] A.D. Maynard, R.J. Aitken, T. Butz, V. Colvin, K. Donaldson, G. Oberdoerster, M.A. Philbert, J. Ryan, A. Seaton, V. Stone, S.S. Tinkle, L. Tran, N.J. Walker, D.B. Warheit, Nature 444 (2006) 267–269.
[12] X. Lin, T. Huang, F. Huang, W. Wang, J. Shi, J. Mater. Chem. 17 (2007) 2145–2150.
[13] L.-M. Yang, G.-Y. Zhang, H.-R. Wang, X. Bai, X.-Q. Shen, J.-W. Liu, D.-Z. Gao, CrystEngcomm. 18 (2016) 3683–3695.
[14] Z. Ni, Y. Sun, Y. Zhang, F. Dong, Appl. Surf. Sci. 365 (2016) 314–335.
[15] Y.-S. Xu, W.-D. Zhang, Appl. Catal. B: Environ. 140 (2013) 306–316.
[16] Y. Zhou, Z. Zhao, F. Wang, K. Cao, D.E. Doronkin, F. Dong, J.-D. Grunwaldt, J. Hazard. Mater. 307 (2016) 163–172.
[17] T. Selvamani, B.G.S. Raj, S. Anandan, J.J. Wu, M. Ashokkumar, Phys. Chem. Chem. Phys. 18 (2016) 7768–7779.
[18] Q. Li, X. Hao, X. Guo, F. Dong, Y. Zhang, Dalton Trans. 44 (2015) 8805–8811.
[19] W. Shan, Y. Hu, Z. Bai, M. Zheng, C. Wei, Appl. Catal. B: Environ. 188 (2016) 1–12.
[20] Y. Ao, L. Xu, P. Wang, C. Wang, J. Hou, J. Qian, Dalton Trans. 44 (2015) 11321–11330.
[21] N. Liang, M. Wang, L. Jin, S. Huang, W. Chen, M. Xu, Q. He, J. Zai, N. Fang, X. Qian, ACS Appl. Mater. Inter. 6 (2014) 11698–11705.
[22] C. Ding, F. Cao, L. Ye, K. Liu, H. Xie, X. Jin, Y. Su, Phys. Chem. Chem. Phys. 17 (2015) 23489–23495.
[23] G. Zhu, Y. Liu, M. Hojamberdiev, J. Han, J. Rodriguez, S.A. Bilmes, P. Liu, New J. Chem. 39 (2015) 9557–9568.
[24] D. Sarkar, C.K. Ghosh, S. Mukherjee, K.K. Chattopadhyay, ACS Appl. Mater. Inter. 5 (2013) 331–337.
[25] H. Lv, L. Ma, P. Zeng, D. Ke, T. Peng, J. Mater. Chem. 20 (2010) 3665–3672.
[26] J. Hu, Y. Xie, X. Zhou, J. Yang, J. Alloy. Compd. 676 (2016) 320–325.
[27] S.H. Xu, D.L. Feng, W.F. Shangguan, J. Phys. Chem. C. 113 (2009) 2463–2467.
[28] X. Zhu, F. Zhang, M. Wang, J. Ding, S. Sun, J. Bao, C. Gao, Appl. Surf. Sci. 319 (2014) 83–89.
[29] Xuan Guo, Haojun Zhu, Q. Li, Appl. Catal. B: Environ. 160-161 (2014) 408–414.
[30] Q. Wu, G. Mul, R. van de Krol, Energy Environ. Sci. 4 (2011) 2140–2144.
[31] F. Dong, A. Zheng, Y. Sun, M. Fu, B. Jiang, W.-K. Ho, S.C. Lee, Z. Wu, CrystEngComm. 14 (2012) 3534–3544.
[32] M. Segall, P.J.D. Lindan, M.J. Probert, C.J. Pickard, P. Hasnip, S.J. Clark, M.C. Payne, J. Phys.: Condens. Mat. 14 (2002) 2717–2744.
[33] J.P. Perdew, K. Burke, M. Ernzerhof, Phys. Rev. Lett. 77 (1996) 3865–3868.
[34] I. Ibrahim, I.O. Ali, T.M. Salama, A.A. Bahgat, M.M. Mohamed, Appl. Catal. B: Environ. 181 (2016) 389–402.
[35] F. Wang, Z. Zhao, K. Zhang, F. Dong, Y. Zhou, CrystEngComm. 17 (2015) 6098–6102.
[36] P. Madhusudan, J. Yu, W. Wang, B. Cheng, G. Liu, Dalton Trans. 41 (2012) 14345.
[37] P. Madhusudan, J. Zhang, B. Cheng, G. Liu, CrystEngComm. 15 (2013) 231–240.
[38] S. Shamaila, A.K.L. Sajjad, F. Chen, J. Zhang, Appl. Catal. B: Environ. 94 (2010) 272–280.
[39] F. Dong, S.C. Lee, Z. Wu, Y. Huang, M. Fu, W.K. Ho, S. Zou, B. Wang, J. Hazard. Mater. 195 (2011) 346–354.
[40] R. Dom, A.S. Chary, R. Subasri, N.Y. Hebalkar, P.H. Borse, Int. J. Energy Res. 39 (2015) 1378–1390.
[41] H. Li, T. Hu, R. Zhang, J. Liu, W. Hou, Appl. Catal. B: Environ. 188 (2016) 313–323.
[42] Z. Zhang, C. Shao, X. Li, Y. Sun, M. Zhang, J. Mu, P. Zhang, Z. Guo, Y. Liu,

Nanoscale 5 (2013) 606–618.
[43] Shurong Wang, Jingxv Zhang, Jiedi Yang, Xueling Gao, Hongxin Zhang, Yanshuang Wang, Z. Zhu, RSC Adv. 5 (2015) 10048–10057.
[44] K.S.W. Sing, D.H. Everett, R.A.W. Haul, L. Moscou, R.A. Pierotti, J. Rouquerol, T. Siemieniewska, Pure Appl. Chem. 57 (1985) 603–619.
[45] Y. Huang, W. Fan, B. Long, H. Li, F. Zhao, Z. Liu, Y. Tong, H. Ji, Appl. Catal. B: Environ. 185 (2016) 68–76.
[46] Z. Zhao, Y. Zhou, F. Wang, K. Zhang, S. Yu, K. Cao, ACS Appl. Mater. Inter. 7 (2015) 730–737.
[47] S. Boumaza, A. Boudjemaa, A. Bouguelia, R. Bouarab, M. Trari, Appl. Energy 87 (2010) 2230–2236.
[48] M. Long, P. Hu, H. Wu, J. Cai, B. Tan, B. Zhou, Appl. Catal. B: Environ. 184 (2016) 20–27.
[49] Y. Huang, Y. Liang, Y. Rao, D. Zhu, J.J. Cao, Z. Shen, W. Ho, S.C. Lee, Environ. Sci. Technol. 51 (2017) 2924–2933.
[50] S. Wang, S. Lin, D. Zhang, G. Li, M.K.H. Leung, Appl. Catal. B: Environ. 215 (2017) 85–92.
[51] G. Li, Z. Lian, W. Wang, D. Zhang, H. Li, Nano Energy 19 (2016) 446–454.
[52] Q. Tian, J. Zhuang, J. Wang, l. Xie, P. Liu, Appl. Catal. A: Gen. 425-426 (2012) 74–78.
[53] J. Ma, C. Wang, H. He, Appl. Catal. B: Environ. 184 (2016) 28–34.